A&A 411, 149–156 (2003)
DOI: 10.1051/0004-6361:20031314

Astronomy & Astrophysics

On the intrinsic shape of molecular clouds

C. R. Kerton[1,⋆], C. M. Brunt[1,2,⋆⋆], C. E. Jones[3], and S. Basu[3]

[1] National Research Council of Canada, Herzberg Institute of Astrophysics, Dominion Radio Astrophysical Observatory,
PO Box 248, Penticton, BC V2A 6J9, Canada
[2] Department of Physics and Astronomy, University of Calgary, 2500 University Dr. NW, Calgary, AB T2N 1N4, Canada
[3] Department of Physics and Astronomy, University of Western Ontario, London, ON N6A 3K7, Canada

Received 3 June 2003 / Accepted 14 August 2003

Abstract. Knowledge of the intrinsic shape of molecular clouds and molecular cloud cores provides useful information on both the formation and collapse mechanisms associated with the objects and on the initial conditions for star formation. We compare the shapes of molecular clouds as determined by the Heyer et al. (2001, HCS01) and Brunt et al. (2003, BKP03) catalogues of ^{12}CO($J = 1 - 0$) emission in the outer Galaxy. The catalogues are based upon different versions of the FCRAO Outer Galaxy Survey and also utilize different techniques for defining both the extent and shape of the clouds, which allows us to examine the effects of using different cloud definition and shape-fitting algorithms. In order to compare the two catalogues we use a subset of the cloud population where the clouds are well-defined in both data sets. We model the clouds in terms of triaxial ellipsoids and use a Monte Carlo technique to determine the best-fit intrinsic shape distribution which matches the observed axis ratio distributions. Our analysis shows that the observed shapes of molecular clouds can be best described in terms of an intrinsic distribution of triaxial ellipsoids that are intermediate between near-oblate and near-prolate ellipsoids. The lack of high axis ratio clouds seen in the HCS01 catalogue is shown to be an artifact of the cloud definition algorithm and not an intrinsic property of the molecular clouds.

Key words. ISM: molecules – radio lines: ISM – methods: data analysis

1. Introduction

Jones & Basu (2002, JB02) and Jones et al. (2001, JBD01) investigated the intrinsic shape of molecular clouds and molecular cloud cores over a wide range of size scales (~0.01 pc to 50 pc) and as observed in a variety of tracers including ^{12}CO ($J = 1 - 0$) emission, optical extinction, and submillimetre continuum emission. Knowledge of the intrinsic shapes of such objects provides useful information on both the formation and collapse mechanisms associated with the objects and on the initial conditions for the subsequent formation of stars (e.g., Basu 2000).

One intriguing result that emerged from the JB02 paper was that the larger-scale molecular cloud structures, traced in ^{12}CO($J = 1 - 0$) emission (CO clouds hereafter), had distinctively different distribution of observed axis ratios (p) from the smaller-scale molecular cores and Bok globules. The CO cloud histogram had a strong peak at $p \sim 0.3$ and a distinct lack of clouds with $p > 0.6$. The Monte Carlo simulations of JB02 (described briefly in Sect. 3.3) show that the observed distribution is best-fit by an intrinsic shape distribution of near-prolate clouds, but the low number of clouds with $p > 0.6$ was poorly fit and remained unexplained by JB02. In contrast, the smaller-scale molecular cores and Bok globules were best described by near-oblate triaxial objects. It was suggested by JB02 that this difference may be a reflection of the formation mechanism for the larger scale molecular clouds, with the near-prolate shape arising as a result of the collision of turbulent flows in the interstellar medium (ISM).

As this result was based upon a single CO data set, the Heyer et al. (2001, HCS01) catalogue of CO clouds observed by the Five College Radio Astronomy Observatory (FCRAO) Outer Galaxy Survey (Heyer et al. 1998, OGS), it was recognized by JB02 that the result should be tested against other available CO data sets. Recently a new catalogue based upon a reprocessed version of the FCRAO OGS data has been published (Brunt et al. 2003, BKP03) which uses different techniques than HCS01 to define both the extent and shapes of the CO clouds. The effects of using different cloud shape fitting algorithms used can thus be investigated. Our comparative analysis of the two versions of the OGS data and the two derived catalogues shows that the CO clouds can be best described as triaxial ellipsoids that are neither near-prolate nor near-oblate and also explains why clouds with $p > 0.6$ are under-represented in the HCS01 catalogue. We also demonstrate the advantages and disadvantages of the two shape

---

Send offprint requests to: C. R. Kerton,
e-mail: `charles.kerton@nrc.gc.ca`

[⋆] *Present address:* Department of Physics and Astronomy, Iowa State University, Ames, IA 50011, USA.

[⋆⋆] *Present address:* Department of Astronomy, University of Massachusetts, Amherst, MA 01003, USA.

fitting techniques and, more importantly, show the cases in which each technique fails to provide a good description of the observed cloud shape. In the next section we provide a description of the two cataloged data sets derived from the OGS. In Sect. 3 we describe the cloud shape fitting algorithms and provide a summary of the Monte Carlo modeling technique used to determine the intrinsic cloud shapes. The results of our comparison of the BKP03 and HCS01 data are presented in Sect. 4. A discussion and conclusions follow in Sects. 5 and 6.

2. Data

The original FCRAO OGS was used as the input data set for the HCS01 catalogue. It covers the Galactic area $102^\circ\!.49 < l < 141^\circ\!.54$, $-3^\circ\!.03 < b < 5^\circ\!.41$, and the velocity range $-152 < \mathrm{V}_{\mathrm{lsr}} < 40\ \mathrm{km\,s^{-1}}$, at $45''$ spatial resolution sampled every $50''\!.22$ and $0.98\ \mathrm{km\,s^{-1}}$ velocity resolution ($1.39\ \mathrm{km\,s^{-1}}$ for $l < 106^\circ$) sampled every $0.81\ \mathrm{km\,s^{-1}}$. The typical sensitivity of the OGS at these resolutions is 0.6 K (T_{R}^* scale; all subsequent values will be on this scale unless otherwise noted)

As part of its incorporation into the Canadian Galactic Plane Survey (Taylor et al. 2003, CGPS) the OGS was reprocessed and convolved to $100''\!.44$ spatial resolution (twice the sampling rate). The reprocessing primarily removed correlated noise signals induced by the sharing of reference measurements, as described in Heyer et al. (1998), and suppressed the occurrence of negative signal (up to $\sim$0.5 K levels) in the data arising from unclean reference position measurements. The typical sensitivity of the reprocessed OGS data is 0.17 K due to both the lowered spatial resolution and improvements induced by the reprocessing. The input data for the BKP03 catalogue was the reprocessed OGS with $100''\!.44$ spatial resolution on a $50''\!.22$ spatial grid and a $0.824\ \mathrm{km\,s^{-1}}$ spectroscopic grid (the CGPS standard; see Higgs 1998) covering $-120 < \mathrm{V}_{\mathrm{lsr}} < +20\ \mathrm{km\,s^{-1}}$.

3. Determining intrinsic cloud shapes

In this section we outline how one goes from the observed *lbv* CO data cube to a determination of the intrinsic shapes of the CO clouds. The different techniques used by HCS01 and BKP03 for both cloud definition and cloud shape fitting are compared, and the Monte Carlo modeling technique of JB02 is reviewed briefly.

3.1. Cloud definitions

Obviously the first step is to define a CO cloud. For large-scale structures the most common technique is to define a connected structure in *lbv* space where the voxels are above some chosen intensity threshold. The HCS01 catalogue defined a CO cloud as a continuous structure in *lbv* space above a temperature threshold of $T_{\mathrm{MB}} = 1.4$ K ($\sim$1 K T_{R}^*) extending over a minimum of two contiguous velocity channels and five angular pixels. This definition yielded a total of 10156 clouds.

The main drawback to the basic thresholding technique is that extremely large structures are often defined that are physically unrelated (see Sect. 2 of BKP03 for examples). The goal of the BKP03 catalogue was to construct a catalogue that would be useful for comparison with other large catalogues such as the IRAS Point Source Catalogue and the numerous compilations of high-density molecular line tracers. Therefore, a finer partitioning of the reprocessed OGS was desired. To achieve this, the BKP03 catalogue was constructed using a two-step algorithm. First, all continuous *lbv* structures consisting of at least 4 voxels with $T_{\mathrm{R}}^* > 0.8$ K were identified (note the lower temperature threshold compared with HCS01), resulting in 9489 clouds. The second step of the algorithm further decomposed when possible these (sometimes very large) structures into small regions of localized CO emission enhancements using an enhanced version of the CLUMPFIND algorithm (Williams et al. 1994, CLUMPFIND-clouds hereafter). The majority of the initial clouds (8783 of 9489) actually were not further decomposed by the second step of the algorithm and we refer to these clouds as singular clouds. The remaining 706 "multiple clouds" were decomposed into 5809 CLUMPFIND-clouds by the second stage of the algorithm. In total BKP03 identify 14592 (8783+5809) clouds.

One may be surprised that that BKP03 technique does not lead to an even larger number of clouds compared with the HCS01 technique. Although HCS01 only examines connected objects, these objects get broken up because of the higher temperature threshold (accentuated by requiring two contiguous velocity channels). The first step of BKP03 results in fewer connected *lbv* objects, because of the lower temperature threshold, but these objects are subsequently broken up in the second step of the algorithm.

3.2. Shape fitting algorithms

The next step is to determine the shape of the velocity-integrated cloud image. Both HCS01 and BKP03 describe the shape of a CO cloud in terms of elliptical fits with a major and minor axis diameter, but different algorithms are used. In this subsection we first describe the two algorithms and then demonstrate how they can lead to markedly different results on the same CO cloud.

HCS01 first determine the largest angular separation between the all of the pixels in the velocity integrated image of the cloud (l_{max}). A minimum diameter (l_{min}) is then chosen such that the area of an ellipse with angular diameters l_{max} and l_{min} matches the observed area of the velocity integrated cloud. The HCS01 shape-fitting technique (ellipse-fitting hereafter) is often good for a large-scale description of the cloud shape as it implicitly assigns equal weight to all parts of the cloud. The main drawback of the technique is that, because it treats all points of the cloud equally, it is strongly influenced by the details of the structure of the cloud edges (e.g., see Fig. 1). In most cases like this, the derived l_{max} is a poor description (too large) of the cloud and too low an axis ratio is derived.

In contrast BKP03 used a 2D Gaussian fitting routine[1] (Gaussian-fitting hereafter) and the fitted FWHM values were used to calculate axis ratios. BKP03 attempted to account for the effects of both beam smoothing and truncation by

---

[1] mpfit2dpeak, by C. B. Markwardt.

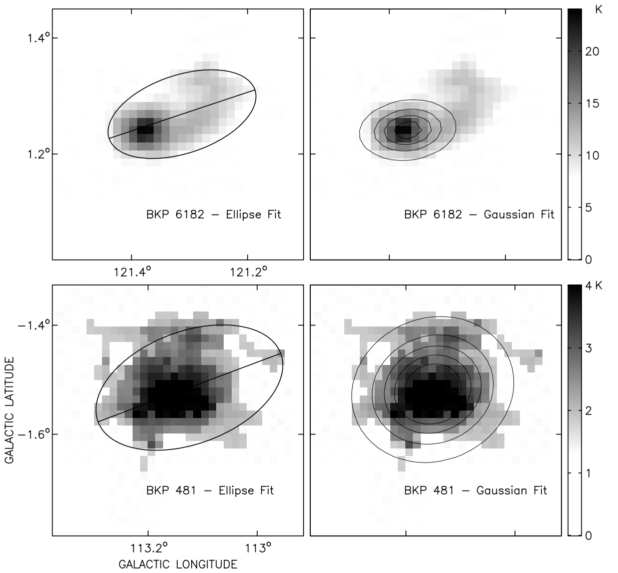

Fig. 1. Cloud shape algorithm differences. The primary difference between the Gaussian-fitting (used in BKP03) and the ellipse-fitting (used in HCS01) techniques is in how the outlying portions of the cloud are handled. The upper two panels show the different fits to the cometary CO cloud BKP 6182. The ellipse-fitting algorithm includes the low-intensity tail of the cloud while the Gaussian fit is drawn to the high-intensity head. In contrast the lower two panels show the more symmetric cloud BKP 481. In this case the ellipse-fitting algorithm is drawn to a very tenuously associated extension of the cloud while the same extension is essentially ignored by the Gaussian-fitting algorithm. In each case only voxels associated with the clouds are shown. Images are all from the reprocessed OGS.

deriving correction factors to the derived major and minor axis fits of the clouds. Corrections were only made for clouds having $T_{\rm peak} \geq 1.6$ K, thus insuring that the half-maximum point of the fit lies above the threshold level. As the Gaussian-fitting technique places more weight on high-intensity areas of the clouds it is good for tracing smaller scale structure and facilitating comparisons with higher density molecular-line tracers. The drawback of the technique is that it provides a poor global fit when there is a marked asymmetry in the distribution of bright and more diffuse emission.

The essential difference between the two techniques arises due to the different ways the algorithms handle outlying points in a cloud. The ellipse-fitting technique places equal weight on each point in the velocity integrated image while the Gaussian-fitting technique places lower weight on the lower intensity edges of the cloud. Figure 1 illustrates this using two BKP03 clouds as examples. Cloud BKP 6182 (upper two panels) has a ellipse-fitting axis ratio of 0.50 and a Gaussian-fitting axis ratio of 0.60. One can see that the Gaussian fit is drawn towards the peak part of the cloud and ignores the northwest extension of the cloud. In contrast BKP 481(lower two panels) is an example of a case where the ellipse-fitting algorithm gets fooled by a the tattered edge of an otherwise very symmetric cloud. The tenuously attached extension of the cloud around $l = 113°$, $b = 1\overset{\circ}{.}45$ deg causes the ellipse-fitting algorithm to select a large major axis, which when combined with the area of the cloud results in a low axis ratio ($p = 0.58$). The Gaussian-fitting technique places a low weight on the low intensity extensions and a much large axis ratio ($p = 0.87$) is derived. Although both of the effects illustrated in the figure result in larger axis ratios for the Gaussian-fitting technique, this is not always the case: horseshoe shaped clouds will often have an ellipse fit that is rounder than the corresponding Gaussian fit (although in this case neither algorithm gives a sensible result). Note also that discrepant fits can occur even for large well-defined clouds.

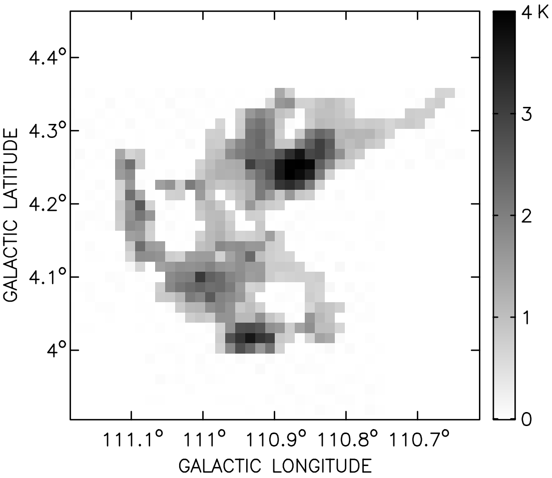

Fig. 2. Velocity integrated image of the CO cloud BKP 455. This large singular cloud (defined by simple *lbv* thresholding) exhibits a complex velocity-integrated structure that is poorly described in terms of either elliptical or Gaussian fits.

Inspection of a collection of velocity-integrated images reveals a large number of CO clouds with very complicated velocity-integrated structure which defy any simple description in terms of ellipsoidal fits. For example, Fig. 2 shows the singular BKP03 cloud BKP 455 that has a particularly complicated velocity-integrated structure. One can ignore the substructures and just say the cloud is generally thin, or one can say the cloud is essentially round with some sections missing. Both descriptions are "correct" in some ways, but clearly a description in terms of axis ratios fails to capture the true complexity of the defined structure. We will return to our interpretation of such structures at the end of this paper.

3.3. Monte Carlo simulations

In this subsection we provide a very brief summary of the Monte Carlo technique used to determine the true shape distribution of the clouds. Details of the technique can be found in JB02 and JBD01. We model the observed axis ratio distribution as being the result of viewing a collection of triaxial ellipsoids from a range of viewing angles. In general, a triaxial ellipsoid can be described by the equation

$$x^2 + \frac{y^2}{\zeta^2} + \frac{z^2}{\xi^2} = a^2, \tag{1}$$

where a is a constant and $1 \geq \zeta \geq \xi$. The apparent axis ratio in projection, p, is known analytically for any viewing angle (Binney 1985).

In order to find the best-fit intrinsic distributions of ζ and ξ, Gaussian distributions of axis ratios with peak values ζ_0 and ξ_0 and standard deviation (σ) typically $= 0.1$ are input into a Monte Carlo program. We use 10^4 viewing angles to calculate the distribution of projected axis ratios p from each pair of intrinsic axis ratios, and 10^4 sets of axis ratios in each Gaussian distribution. The program produces the expected observed distribution of p which can then be compared with the observed distribution via a χ^2 analysis. Minimization of the χ^2 values yields the best fit ζ_0 and ξ_0. JB02 point out that distributions of triaxial shapes where $\zeta_0 = \xi_0$ emphasize prolate objects, while distributions with ζ_0 near 1 emphasize oblate objects. Also if $\zeta_0 > \frac{1}{2}(1 + \xi_0)$ then the distribution can be said to contain more nearly oblate than nearly prolate objects.

4. Comparing BKP03 and HCS01

Given the differences between both the BKP03 and HCS01 input data and the cloud extraction and definition techniques it is a non-trivial task to select a meaningful sample to compare the two catalogues. Our approach is to select a subsample of clouds that are fairly well understood and then use those to draw conclusions about the entire population of clouds.

The starting point for the BKP03 subsample is the *lbv* threshold-defined singular clouds along with the multiple clouds which broke up into 2–10 sub-objects in the second stage of the algorithm (this accounts for 99.5% of the threshold-defined clouds). The 2–10 sub-object limit was chosen to avoid the pathological multiple clouds that are clearly interconnected unrelated emission. To reduce the uncertainty caused by the fitting techniques we then select only those clouds for which the uncorrected Gaussian and ellipse axis ratio fits agree to within 0.083 (the axis ratio bin size used in JB02). Inspection of a number of these clouds supports the idea that these clouds are well described by the Gaussian-fitting technique and we are thus able to correct the Gaussian fits for beam smoothing and truncation. Finally, as was done by JB02, we restricted the analysis to those clouds with $N_s > 10$, where N_s is the number of spatial pixels in the velocity-integrated cloud image. Physically, this means the smallest clouds in the sample have diameters of about 0.5 pc. The final subsample meeting all of our criteria has 818 singular clouds and 227 multiple clouds. While this is a marked reduction from the total number of clouds in the BKP03 catalogue we emphasize that the subsample represents those clouds which have been extracted using *lbv* thresholding, have velocity-integrated images well described in terms of ellipsoids, and can be corrected for beam smoothing and truncation effects. By examining this “well-behaved” subset we hope to gain some insight into the nature of the more complex objects.

We begin by examining the 818 singular clouds. The histogram of the corrected BKP03 axis ratios is shown in Fig. 3 along with a scaled version of the HCS01 sample from JB02. Two things are readily apparent, the histogram is not as sharply peaked as the HCS01 histogram, and the BKP03 histogram includes a substantial population of clouds with $p > 0.6$.

Since the reprocessed OGS has a lower resolution than the original OGS we first want to demonstrate that the beam and truncation corrections derived for the BKP03 catalogue do indeed allow a meaningful comparison with the HCS01 data. In order to explore this further we attempted to match clouds from the HCS01 catalogue with the 818 singular BKP03 clouds by searching for clouds with measured centroid positions within $0\overset{\circ}{.}03$ spatially and 0.1 km s^{-1} in velocity. In total we obtained 229 unique matches. Matches were obtained across the full axis ratio distribution, and the matched cloud histogram is essentially a scaled-down version of the histogram shown in Fig. 3.

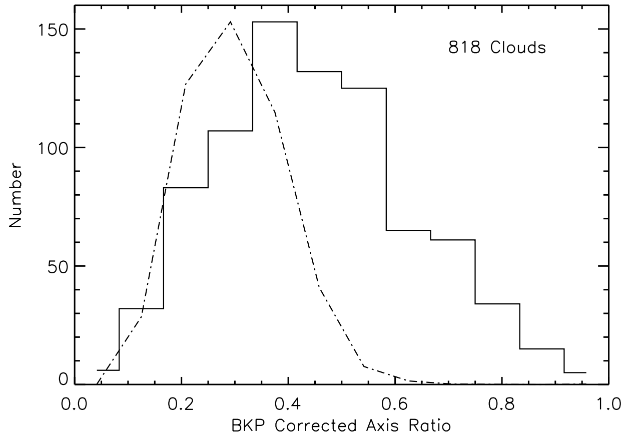

Fig. 3. Singular cloud histogram. The distribution of axis ratios (BKP03 corrected fits) for the 818 singular clouds with matching Gaussian and ellipse fits is shown as the solid-line histogram. For shape comparison a scaled version of the HCS01 sample from JB02 is shown as the dot-dash line.

The original OGS data were first regridded in velocity space to match the reprocessed OGS grid and, for each matched cloud, the same pixels were extracted from the original OGS as were extracted from the reprocessed OGS. Gaussian fits were then made to the extracted original OGS data. Figure 4 shows the uncorrected axis ratios determined from Gaussian fits to the matched clouds in the original and the reprocessed OGS data. As expected the axis ratios of the clouds as seen in the reprocessed OGS tend to be larger than when they are observed in the original OGS. Figure 5 shows the corrected axis ratio fits. In this case the reprocessed OGS data have been corrected for truncation and beam smearing and the original OGS data have been corrected for a 45″ beam. We see there is a very good match between the axis ratios determined using the two data sets. This demonstrates that the corrected Gaussian fits to the reprocessed OGS data do provide a measurement of the cloud axis ratio that is similar to what would be obtained using beam corrected original OGS data.

Another concern is that the fixed angular resolution of the observations may bias the observed axis ratios. For example, one might expect that more distant molecular clouds may have larger axis ratios than closer molecular clouds simply due to the fact they have a smaller angular extent. In Fig. 6 we have plotted the corrected BKP03 Gaussian fits for the 818 clouds as a function of their peak $V_{\rm lsr}$. The only pattern visible in this plot is due to the spiral structure of the Galaxy, with the division between local clouds (>-20 km s^{-1}) and those at Perseus Arm distances and beyond readily apparent. There is no systematic

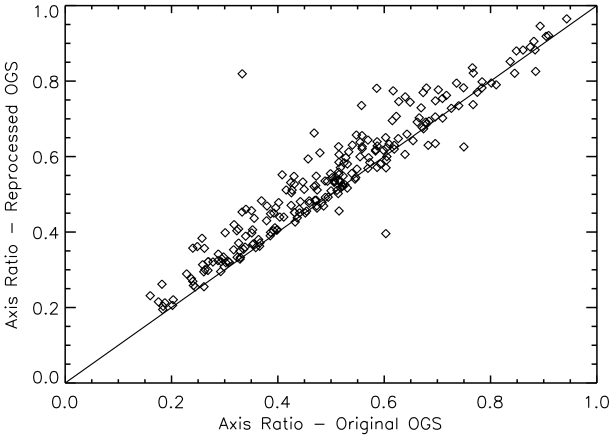

Fig. 4. Raw axis ratio comparison. Raw axis ratios determined from 2D Gaussian fits are shown for matched clouds from the HCS01 and BKP03 catalogue. Note that the raw axis ratios determined using the reprocessed OGS data tend to be larger than the axis ratios determined from the original OGS data. The solid line is the 1:1 line.

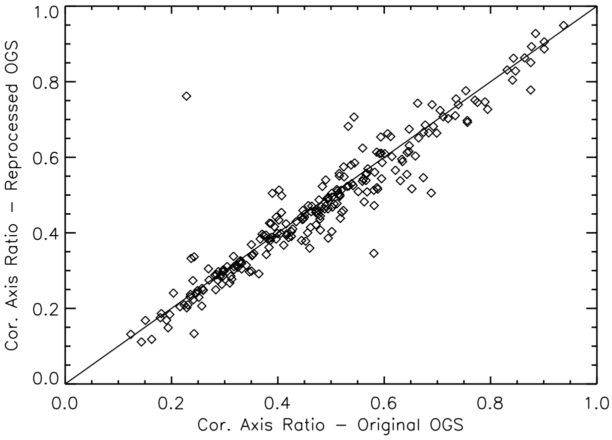

Fig. 5. Corrected axis ratio comparison. As in Fig. 4 but for corrected axis ratios. Fits from the reprocessed OGS have been corrected for beam smearing (100.″44 beam) and truncation, while fits based upon the original OGS have been corrected for a 45″ beam. The solid line is the 1:1 line.

trend in axis ratio with $V_{\rm lsr}$. In Fig. 7 we have replotted the histogram shown in Fig. 3 along with histograms of the axis ratios of local clouds ($V_{\rm lsr}$.> -20 km s^{-1}) and Perseus Arm clouds (-60 km s^{-1} < $V_{\rm lsr}$ < -30 km s^{-1}). We see that clouds at all distances contribute to all parts of the axis ratio distribution.

Returning to the observed distribution of axis ratios for the entire sample of 818 clouds, the Monte Carlo algorithm yields best-fit mean axis ratios $\xi_0 = 0.3 \pm 0.1$ and $\zeta_0 = 0.6 \pm 0.1$ (Table 1 summarizes all of the Monte Carlo results from this paper along with a couple of results from JB02 for comparison). These parameters correspond to an intrinsic triaxial distribution for the singular clouds that can be described as a distribution of triaxial ellipsoids which are intermediate between near-oblate and near-prolate objects.

Next we examine the 227 multiple clouds. As would be expected, given how these clouds are defined, these clouds also tend to be larger than the singular clouds. A total of 88% of the singular clouds have $N_s < 100$ while only 22% of the multiple cloud sample has $N_s < 100$. Figure 8 shows the histogram for these clouds again along with a scaled version of the HCS01 data histogram. The BKP03 multiple cloud distribution is similar to the HCS01 distribution at low axis ratios, but it is slightly broader and has a much more significant $p > 0.4$ tail. The best-fitting triaxial distribution for the multiple clouds has $\xi_0 = 0.3 \pm 0.1$ and $\zeta_0 = 0.3 \pm 0.1$ – dominated by near-prolate objects.

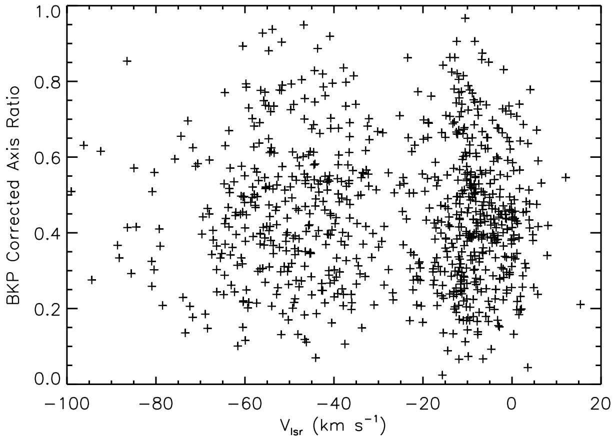

Fig. 6. Variation of axis ratio with $V_{\rm lsr}$. The BKP corrected axis ratios are plotted as a function of the peak $V_{\rm lsr}$ of the cloud. No systematic trend of axis ratio with velocity is observed. Note the clear separation of the local clouds ($V_{\rm lsr}$.> -20 km s^{-1}) from more distant Perseus Arm and far outer Galaxy clouds.

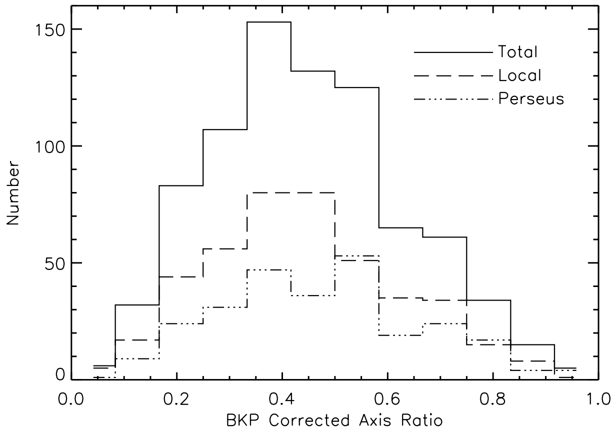

Fig. 7. Singular cloud histogram – Local and Perseus Arm clouds. The solid line shows the histogram from Fig. 3. Histograms for subsamples of local clouds ($V_{\rm lsr}$.> -20 km s^{-1}) and Perseus Arm clouds (-60 km s^{-1} < $V_{\rm lsr}$ < -30 km s^{-1}) are also shown as dashed and dot-dashed lines respectively. Note that both the local and Perseus Arm subsamples contain the full range of axis ratios.

In Fig. 9 we show the combined singular and multiple cloud histogram. This represents our best sample of threshold-defined clouds which are insensitive to the choice of shape fitting algorithm and as such defines the best sample from BKP03 for determining the intrinsic shape distribution of the clouds. The best-fitting triaxial distribution for the combined sample has $\xi_0 = 0.2 \pm 0.1$ and $\zeta_0 = 0.6 \pm 0.1$, again corresponding to a distribution of triaxial objects which cannot be classified as either near-oblate or near-prolate.

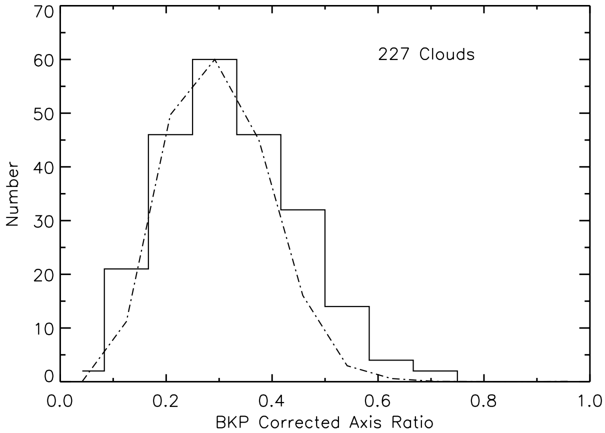

Fig. 8. Multiple cloud histogram. As Fig. 3, but for the multiple clouds consisting of 2–10 substructures.

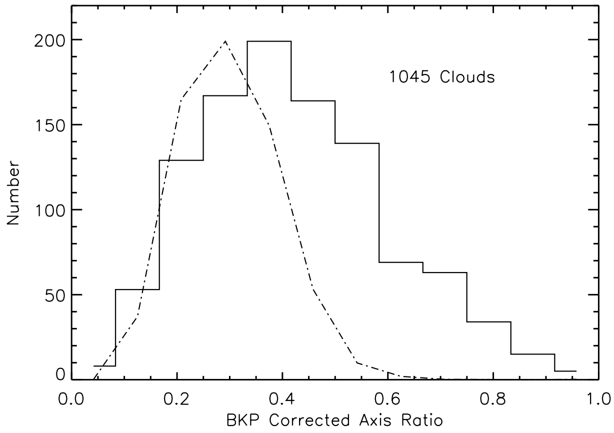

Fig. 9. Combined histogram. As in Figs. 3 and 8, but showing the combination of the singular and multiple cloud axis ratios.

Table 1. Best-fit mean axis ratios.

Sample	ξ_0 (± 0.1)	ζ_0 (± 0.1)
Singular Clouds (Fig. 3)	0.3	0.6
Multiple Clouds (Fig. 8)	0.3	0.3
Combined Sample (Fig. 9)	0.2	0.6
CLUMPFIND-Clouds (Fig. 10)	0.2	0.6
JB02 - HCS01 All Clouds	0.3	0.3
JB02 - Molecular cores/globules	0.4	0.9

5. Discussion

5.1. The elongated shape of molecular clouds

Our analysis of the BKP03 data suggests that molecular clouds are best described in terms of a distribution of ellipsoids that are neither near-oblate nor near-prolate. Only the multiple clouds, which are made up of a number of substructures, are well described in terms of near-prolate ellipsoids. It is interesting to examine the axis ratio distribution of the CLUMPFIND-clouds that make up the substructure of our sample of multiple clouds.

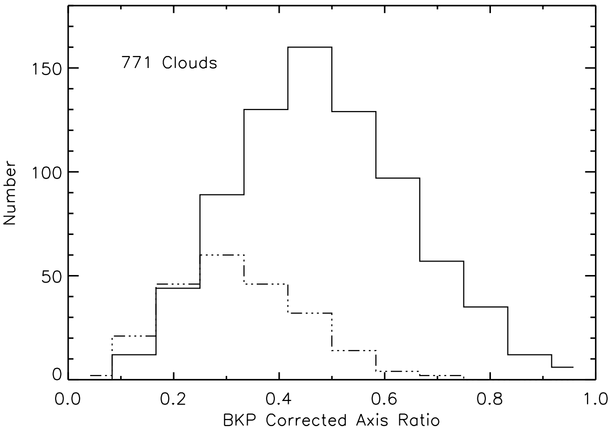

Fig. 10. CLUMPFIND-cloud histogram. The solid-line histogram is for the sample of 771 CLUMPFIND-clouds defined from the original 227 multiple clouds. The multiple-cloud histogram from Fig. 8 is shown in a dot-dash line for comparison.

The original 227 multiple clouds result in 771 CLUMPFIND-clouds that have matching HCS01 and BKP03 axis ratios and have derived correction factors. Figure 10 shows the distribution of the axis ratios for these clouds. The best-fit triaxial distribution has $\xi_0 = 0.3$ and $\zeta_0 = 0.6$, again corresponding to a distribution of triaxial objects that are neither near-oblate nor near-prolate – the substructure within the multiple clouds is best described in the same way as the singular molecular clouds.

Within the restriction of using ellipsoids to describe molecular cloud shapes, the picture that emerges is that of three levels of structure. The majority of molecular clouds are best described with an intrinsic shape distribution of triaxial objects that are neither near-oblate nor near-prolate. The larger multiple clouds, resulting from a superposition of smaller clouds, are better described in terms of a near-prolate dominated shape distribution. Finally, from JB02 and JBD01, the much smaller molecular core structures are best described in terms of a near-oblate dominated shape distribution. Physically, this means that while only the largest observed clouds can be ascribed a prolate, or “filamentary” shape, even these are usually due to a close association of several triaxial clouds in a crowded region. In general, the influence of large-scale turbulence and shock waves in the interstellar medium is likely to lead to more unconstrained shapes, in which no two dimensions of the cloud match each other, as required for purely prolate or oblate objects. However, as self-gravitating dense cores are formed within the clouds, the presence of significant magnetic support can lead to a preferential flattening in *one* direction, that of the mean magnetic field, yielding a near-oblate shape.

Finally, how can one better describe the large-scale clouds? While an prolate ellipsoid does capture the sense of “thinness” often seen in the multiple clouds it omits a wealth of morphological information. Also, as we have demonstrated in Fig. 2, some defined clouds simply cannot be described in terms of ellipsoids. With the availability of high spatial dynamic range surveys of molecular line tracers enabled by the new generations of array receivers combined with increasingly

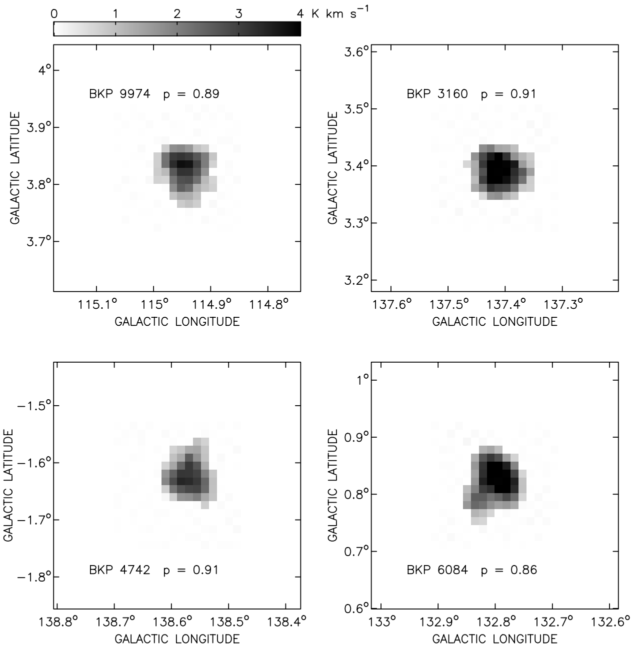

Fig. 11. Round BKP03 clouds. Four examples of round clouds from the reprocessed OGS data as defined by the BKP03 catalogue. These clouds are selected from a sample of clouds that are insensitive to the fitting technique utilized. Only two clouds as round as these ($p > 0.85$) are found in the *entire* HCS01 sample used in JB02.

sophisticated numerical simulations of the ISM the need for the development of new descriptors of cloud morphology is clear.

5.2. On the lack of $p > 0.6$ clouds in the HCS01 sample

It is clear from the histograms shown in Sect. 4 that there are many more high axis ratio CO clouds in the BKP03 data compared with the HCS01 data. For example, in the BKP03 singular cloud subsample (818 clouds) there are a total of 54 clouds with $p > 0.75$ compared with only 3 clouds in the *entire* HCS01 sample examined by JB02 (5685 clouds). Indeed the dearth of these round clouds in the HCS01 distribution was commented on by JB02 as it is difficult to reconcile with any model distribution of ellipsoids. In Fig. 11 we show a few of these round clouds from the BKP03 singular cloud subsample. It is important to note that both elliptical and Gaussian fits give essentially identical results for this subsample and the Gaussian fits have been corrected for beam smearing and truncation.

In Table 2 we show the results of a comparison of the axis ratio fits from the BKP03 and HCS01 catalogues for the matched clouds. As would be expected due to the lack of high p clouds in HCS01 the largest discrepancy between the axis ratios occurs for the clouds with high p clouds in the BKP03 catalogue. We extracted data from the original OGS for a number of the clouds showing a large axis ratio difference (two of these clouds are shown in Fig. 12). The examined original and reprocessed clouds tend to have similar maximum spatial extents but the area of the clouds in the original OGS data is much smaller. In most cases we found that the edges of the high p clouds tend to get lost in the noise of the original OGS data

Table 2. Matched clouds – axis ratio difference.

$\|\Delta p\|^a$	Mean($p_{\rm BKP}$)	Number of Clouds
$0.5 < \|\Delta p\|$	0.88	4
$0.4 < \|\Delta p\| \leq 0.5$	0.78	11
$0.3 < \|\Delta p\| \leq 0.4$	0.71	15
$0.2 < \|\Delta p\| \leq 0.3$	0.56	38
$0.1 < \|\Delta p\| \leq 0.2$	0.47	61
$\|\Delta p\| \leq 0.1$	0.35	100

[a] $\Delta p = p_{\rm BKP03} - p_{\rm HCS01}$.

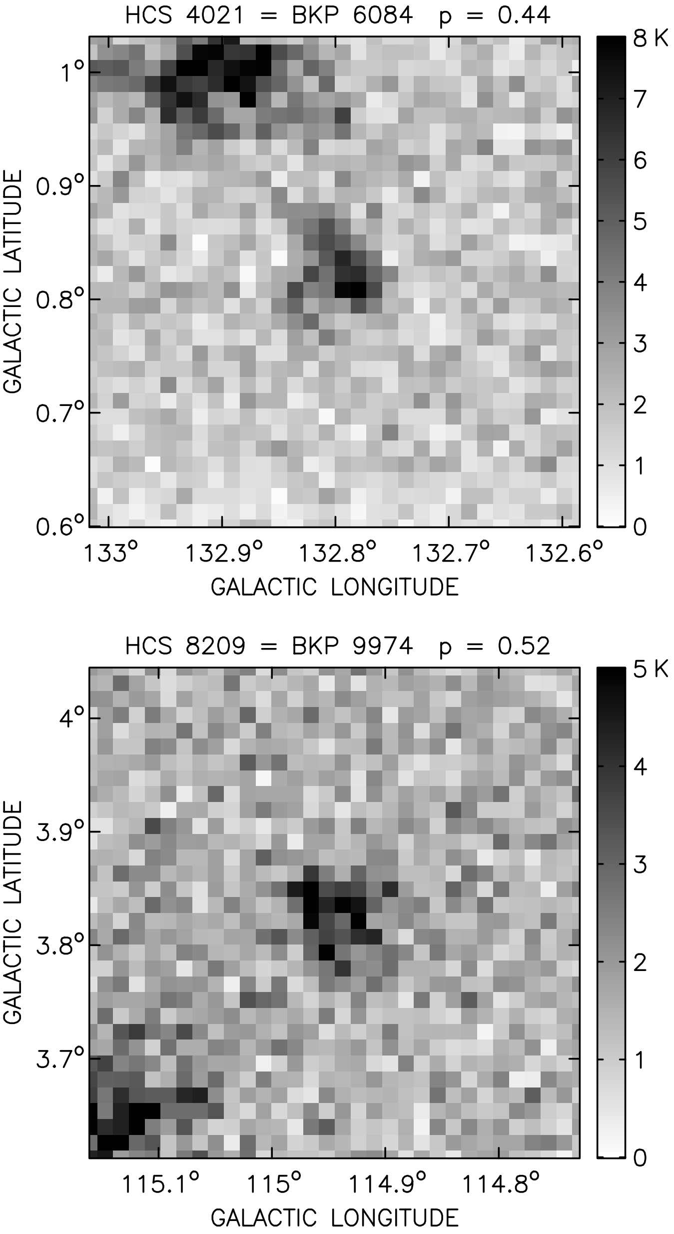

Fig. 12. Matched clouds from the original OGS. Velocity-integrated images of two of the clouds from Fig. 11 are shown here as they appear in the original OGS data. The axis ratio shown above each frame is the HCS01 ellipse fit to the original OGS data. Corrected Gaussian fits to original OGS data extracted using the BKP03 pixel masks yield axis ratios of $p = 0.84$ for HCS 4021 and $p = 0.88$ for HCS 8209.

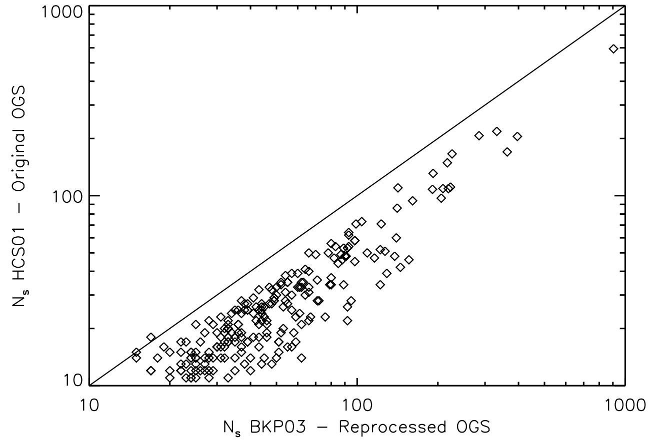

Fig. 13. Spatial pixel comparison. The plot shows the number of spatial pixels contained in the velocity-integrated images of all of the matched clouds. Notice that the BKP03 clouds tend to be larger than the equivalent HCS01 clouds. The solid line is the 1:1 line.

while the smoothed data in the reprocessed OGS allows for a better recovery of these pixels. For example both HCS 4021 and BKP 6084 have approximately the same maximum length (0°.15 and 0°.18 respectively) but $N_s = 57$ for BKP 6084 compared with $N_s = 25$ for HCS 4021. This substantial increase in the number of pixels, combined with very little change in the maximum cloud length, results in a significant change in the axis ratio derived from ellipse-fitting: $p = 0.44$ to $p = 0.81$. In contrast a Gaussian fit is not sensitive to the addition of low intensity pixels and when applied to both the original and reprocessed versions of the cloud results in very similar axis ratios: $p = 0.84$ and $p = 0.86$ respectively. The same behavior is seen for BKP 9974 (HCS 8209): a substantial change in the axis ratio derived from ellipse-fitting and little change if Gaussian-fitting is used. This effect is not restricted to the clouds shown. Figure 13 shows that the BKP03 clouds always tend to have more spatial pixels than their equivalent HCS01 cloud. This reduction in the number of pixels included as part of the cloud results in equivalent clouds being thinner in the HCS01 catalogue. This is because the resulting proportional loss in the area of the cloud tends to be more severe than the reduction in the $l_{\max}$ value so a low $l_{\min}$ is derived to match the lowered area of the cloud, resulting in a lower value for p.

6. Conclusions

(1) The lack of clouds with high observed axis ratios in the original HCS01 catalogue is due to poor recovery of low intensity pixels at the edges of the clouds combined with the sensitivity of the HCS01 fitting technique (ellipse-fitting) to the distribution of outlying points. There is a larger relative change in recovered cloud area than in $l_{\max}$ resulting in a lowered axis ratio. For a subset of matched clouds we have shown that this structure is recovered in the reprocessed OGS.

(2) Unlike the results of JB02 for the HCS01 catalogue, only the very large multiple clouds of BKP03 are well described by a distribution of near-prolate ellipsoids. The sub-structure making up these clouds does not share this shape distribution.

(3) Smaller, singular, molecular clouds and the sub-structures within multiple molecular clouds are best described with an intrinsic shape distribution of triaxial objects that are intermediate between near-oblate and near-prolate ellipsoids.

Acknowledgements. The Canadian Galactic Plane Survey is a Canadian project with international partners, and is supported by the Natural Sciences and Engineering Research Council (NSERC) of Canada. The research of C.B. and S.B. is supported by a grant from NSERC. C.E.J. acknowledges financial support from an NSERC postdoctoral fellowship.

References

Basu, S. 2000, ApJ, 540, L103
Binney, J. 1985, MNRAS, 212, 767
Brunt, C. M., Kerton, C. R., & Pomerleau, C. 2003, ApJS, 144, 47 (BKP03)
Jones, C. E., & Basu, S. 2002, ApJ, 569, 280 (JB02)
Jones, C. E., Basu, S., & Dubinski, J. 2001, ApJ, 551, 387 (JBD01)
Heyer, M. H., Brunt, C., Snell, R. L., et al. 1998, ApJS, 115, 241
Heyer, M. H., Carpenter, J. M., & Snell, R. L. 2001, ApJ, 551, 852 (HCS01)
Higgs, L. A. 1998, in New Perspectives on the Interstellar Medium, ed. A. R. Taylor, T. L. Landecker, & G. Joncas (San Francisco: ASP), ASP Conf. Ser., 168, 15
Taylor, A. R., Gibson, S. J., Peracaula, M., et al. 2003, AJ, 125, 3145
Williams, J. P., de Geus, E., & Blitz, L. 1994, ApJ, 428, 693